17

Hard X-Ray Microoptics

A. Snigirev and I. Snigireva

Abstract. This chapter presents a summary of micro-focusing optics and methods for X-rays in the energy range 4–100 keV, as provided by synchrotron radiation sources. The advent of third generation storage rings such as the ESRF, the APS and Spring-8 with X-ray beams of high brilliance, low divergence and high coherence has made possible efficient X-ray focusing and imaging. The main emphasis is on those methods which aim to produce submicrometre and nanometre spatial resolutions in imaging applications. These methods fall into three broad categories: reflective, refractive and diffractive optics. The basic principles and recent achievements are discussed for optical devices in each of these categories.

17.1 Introduction

A summary of microfocusing optics and methods for hard X-rays is presented. The hard X-ray region is taken as extending from about several keV (∼4 keV) to gamma rays with several hundreds keV (∼100 keV) provided by synchrotron radiation sources. The advent of third generation storage rings like ESRF, APS, and SPring-8 with radiation beams of high brilliance, low divergence, and high coherence makes possible efficient X-ray focusing and imaging. X-ray microscopy techniques are presented first. The main emphasis will be put on those methods that aim to produce nanometer resolution. These methods fall into three broad categories: reflective, refractive, and diffractive optics. The basic principles and recent achievements will be discussed for all optical devices. The report covers the latest status of reflective optics, including mirrors and multilayers, capillaries and waveguides. Special attention will be given for successful development of Kirkpatrick–Baez (KB) systems providing nanometer focusing in two dimensions. The basic principles and the state of the art of diffractive optics such as Fresnel zone plates are reviewed. Improvement of the spatial resolution without loss of efficiency is difficult and incremental due to the fabrication challenges posed by the combination of small outermost zone width and high aspect ratios. Particular attention will be given to recent invention of refractive optics. Refractive optics is a

rapidly emerging option for focusing high energy synchrotron radiation from micrometer to nanometer dimensions. These devices are simple to align, offer a good working distance between the optics and the sample, and are expected to become standard elements in synchrotron beamlines instrumentation in general and in high energy X-ray microscopy in particular.

17.2 X-Ray Microscopy

The history of X-ray microscopy goes back to 1896, the year following the discovery of X-rays by Roentgen. The method used to study the structural details of biological objects by enlargement of X-ray radiographs was called by P. Goby as microradiography in 1913 [1]. Beginning in the late 1940s, X-ray microscopy with grazing incidence mirror optics was proposed by P. Kirkpatrick in order to surpass the optical microscope in resolution [2].

As a branch of earlier developments in electron microscopy, projection microscopy was proposed by Cosslett and Nixon [3] and it became very popular since the 1950s. In the early 1970s, several groups started new technological developments of X-ray optics, in particular, Fresnel zone plates, and the modern era of X-ray microscopy started. In 1974, Schmahl and collaborators built a full-field transmission microscope at DESY (Deutsches Elektronen Synchrotron) in Germany [4]. Kirz and Rarback at NSLS (National Synchrotron Light Source) at Brookhaven National Laboratory in USA built the first scanning transmission microscope using a zone plate objective in 1982 [5]. Traditionally, this type of X-ray microscopy deals with rather soft X-ray energies (100–2,000 eV), in particular, in the so-called water window region between the K-shell X-ray absorption edges of carbon and oxygen at 4.4 and 2.3 nm, where organic materials show strong absorption and phase contrast while water is relatively nonabsorbing. This enables imaging of specimens up to $\sim$10 μm thickness, with high intrinsic contrast using X-rays with a lateral resolution down to 15 nm [6].

In recent years, considerable progress has been made in X-ray microscopy in the hard X-ray regime ($E > 4$ keV), as a result of the development of high brilliance, high energy X-ray sources coupled with advances in manufacturing technologies of focusing optics. One of the key strengths of hard X-ray microscopy is the large penetration depth of hard X-rays into the matter around 1 mm, allowing one to probe the inner structure of an object without the need for destructive sample preparation. Resolution of the order of 100 nm was reached with photon energies up to 30 keV.

Lens-based X-ray microscopy can be divided into two classes: full-field microscopy and scanning microscopy (Fig. 17.1). The full-field transmission X-ray microscope (TXRM) uses the same optical arrangement as conventional light and transmission electron microscopes. Such types of microscopes use optical elements like Fresnel zone plates or refractive optics as objective
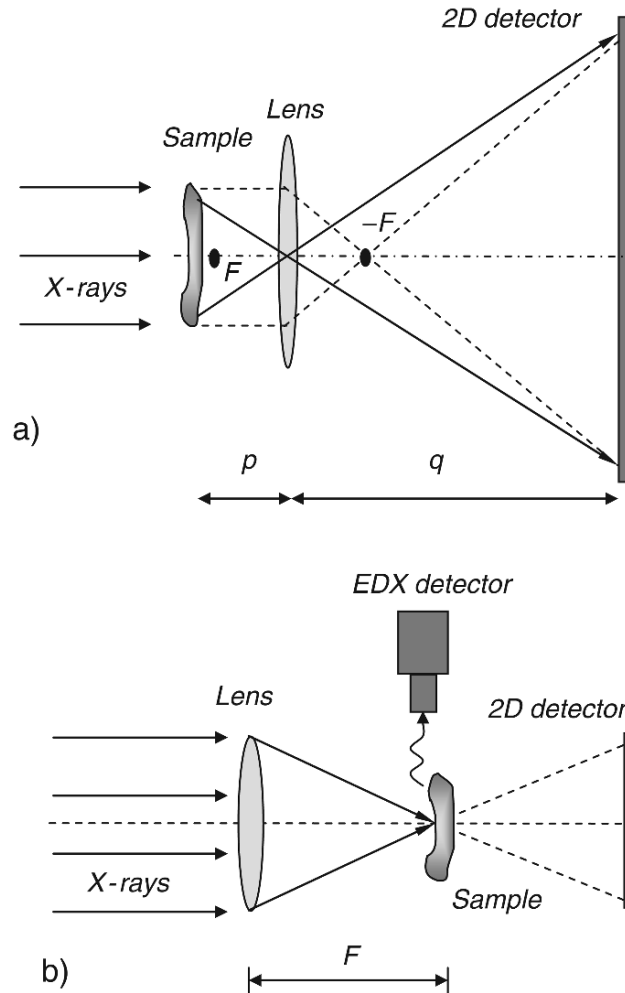
Fig. 17.1. Optical schematic of (**a**) transmission and (**b**) scanning-transmission X-ray microscopes

lenses for high-resolution imaging. Scanning microscopes usually use a focusing optics to form a finely focused spot or microprobe through which the specimen is rastered. The microscope of choice is generally determined by the specimen and observation to be made on it. Table 17.1 summarizes different types of X-ray microscopes available nowadays [7–11].

The full-field transmission microscope is illustrated schematically in Fig. 17.1a. The basic approach is to use a high quality imaging optics as a microscope objective to create a magnified image of the object. When the object is placed slightly outside the focal distance (p is slightly larger than F), then a strongly magnified image is generated at a distance $q = pF/(p - F)$

Table 17.1. Comparison of the features of different types of X-ray microscopy

Type of microscopy		Source	Energy	Mode of contrast	Optics	Resolution (nm)
Full field	Micro-radiography	Contact	SR, Lab	>0.5 keV	Absorption	–	100–1,000
		In-line imaging	SR	>1 keV	Absorption/phase XANES/EXAFS	–	500–1,000
		Magnified projection (no optics)	Lab	>1 keV	Absorption/phase	–	100–500
	Soft X-ray microscopy		SR, Lab	<4 keV	Amplitude/phase XANES	FZP	20–50
	Hard X-ray microscopy		SR, Lab	>4 keV	Amplitude/phase XANES/EXAFS possible	FZP, CRL	100–500
Scanning	Soft X-ray scanning microscopy		SR	<4 keV	Absorption, fluorescence, XANES/EXAFS photoemission	FZP	20–50
	Hard X-ray microprobe		SR, Lab	>4 keV	Absorption, fluorescence, XANES/EXAFS, diffraction	FZP, CRL, KB	100–1,000

Abbreviation: SR synchrotron radiation sources, Lab laboratory based sources, XANES X-ray absorption near edge spectroscopy, EXAFS Extended X-ray absorption fine spectroscopy

with magnification $M = q/p = F/(p-F)$. This technique offers the possibility of dynamic imaging and is well suited for phase contrast imaging.

The basic soft X-ray microscope approach is to use a condenser zone plate to monochromatize and to concentrate X-rays onto the sample. The micro-objective zone plate forms a magnified real image of the sample at roughly $1,000\times$ magnification. The enlarged image is recorded on a backside-thinned CCD camera. The sample is mounted in an environmental chamber where it can be prepared between two thin foils in its natural state, including when wet. The object chamber is under atmospheric pressure, while the major parts of the X-ray optical path are in vacuum. Image exposure times range from under a second with dry specimens to a few seconds for wet specimens, depending on the zone plate used. Phase contrast in TXRM as a full analogue of Zernike phase contrast in visible light microscopy has been realized. A removal ring aperture is placed near the condenser and a phase-ring is permanently mounted in the conjugate plane. The improved contrast allowed for reduced illumination and therefore reduced radiation dose to the specimen. A cryogenic object chamber has been developed and implemented at the TXRM. The cryogenic method allows imaging of chemically unfixed samples with resolution 20–30 nm. Furthermore, the high stability of frozen-hydrated samples allows taking multiple images for tomography.

For hard X-rays, two types of optics are available today with sufficient quality to be used in the development of full-field imaging: Fresnel zone plates (FZPs) and compound refractive lenses (CRLs). Both have in common that their focal length for X-rays with photon energies around 10 keV and higher is in the order of meters, and that their apertures are limited to several hundreds of micrometers. The length of the setup will increase as M increasingly differs from unity. The length of the entire microscope can be of the order of 10–25 m. Another implication of a long focal length is a very small numerical aperture, which limits the resolution of the imaging setup. The resolution of about 100–300 nm is routine now.

X-ray microscopy in the scanning mode is illustrated in Fig. 17.1b. The basic idea in scanning microscopy is to form a microprobe across which the specimen is mechanically scanned. A proportional counter is used to detect the transmitted X-rays and the image is built up pixel (picture element) by pixel. The focused X-ray probe can also be used to excite other processes such as photoelectrons and fluorescent X-rays. The spatial resolution is limited by the focusing optics. Scanning transmission X-ray microscopes (STXRM) for soft X-rays use Fresnel zone plates as high resolution objectives to form a focused spot. Scanning microscopes require coherent illumination and must be used with high brightness sources such as undulators at synchrotron storage rings. Scanning microscopes generally have exposure times of minutes; each pixel can be formed in a few milliseconds using synchrotron radiation. Such microscopes impact 5–10 times less radiation dose onto the specimen and have an energy resolution of 0.1 eV. Scanning transmission X-ray microscopes are better suited to spectromicroscopy. Two main types of

scanning microscopes exist today: STXRMs equipped with photon detectors and scanning photoemission microscopes equipped with electron detectors.

In the case of hard X-rays a microfocus is generated by KB mirrors, a Fresnel zone plate, or a parabolic CRL. The high-energy microfocusing optics benefits from longer focal lengths and a larger depth of field, up to a few millimeters, that is advantageous for the use of specific sample environment like furnaces or high-pressure cells. Shorter wavelengths are favorable for diffraction studies including wide and small angle scattering. In a microprobe, the strategy is to scan the beam over the sample and to measure a signal in diffraction, in fluorescence, or in absorption (XANES, EXAFS) for each beam position. When combining scanning microscopy with tomographic techniques the inner structure of a sample can be reconstructed, including the distribution of different atomic species and even of the valences of atoms.
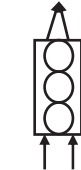
17.3 X-Ray Optics

The small source size and low divergence of third generation synchrotron radiation sources gave rise to tremendous advances in the development of different types of microfocusing optics based on reflection, diffraction, and refraction phenomena. All available microfocusing devices for hard X rays are presented in the Table 17.2. The best resolution for the optical systems presented exceeds the 100 nm limit. From their principles of operation these optical systems are subdivided into the three broad groups.

17.3.1 Reflective Optics

Kirkpatrick–Baez Systems

Conventional mirrors, as used for visible wavelength, at normal incidence cannot be used, because the reflectivity is too low and typically less then one hundred thousand X-ray photons will be reflected. A high reflectivity can, however, be obtained at grazing incidence angles $\left(\theta < \sqrt{\delta}\right)$. To reduce the astigmatism, Kirkpatrick and Baez proposed the use of two spherical or cylindrical mirrors in a crossed configuration [2]. Figure 17.2 shows a geometrical arrangement of such so-called Kirkpatrick–Baez (KB) system. To enhance the reflectivity, multilayer mirrors, where the refractive index varies periodically with depth, can be used. To build such mirrors, alternative layers with a thickness $\lambda/4$ are evaporated or spattered onto a blank one with a relatively high refractive index and the other with a relatively low refractive index. The weak radiation reflected at the interfaces of the multiplayer is superimposed coherently and in phase, and can give a considerably increased reflectivity. The reflecting focusing systems can be either static, with mirrors polished according to the proper figure optimized for a given incidence angle and focus, or

Table 17.2. Microfocusing optics for hard X-rays

	Reflective				Waveguides	Diffractive	Refractive
	Kirkpatrick–Baez systems		Capillaries				
	Mirrors	Multilayers	Multi-bounce	One-bounce		Fresnel zone plates	Refractive lenses
	Kirkpatrik and Baez, 1948	Undewood and Barbee, 1986	Kreger, 1948	Balaic, 1995	Feng et al., 1993	Baez, 1952	Snigirev et al., 1996
E	<20 keV	<80 keV	<20 keV	White beam	<20 keV	<30 keV	<1 MeV
$\Delta E/E$	White beam	10^{-2}	White beam		10^{-3}	10^{-3}	10^{-3}
Δ	36 nm [12]	45 nm [13]	50 nm [14]	250 nm [15]	$40 \times 25\,\mathrm{nm}^2$ [16]	30 nm [17]	50 nm [18]

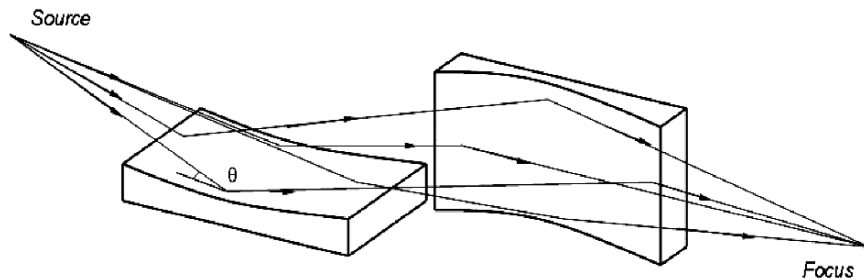E, energy range; $\Delta E/E$, energy bandwidth; Δ, best measured resolution

Fig. 17.2. Schematic view of the two-mirror Kirkpatrick–Baez system. θ is the mirror incidence angle

dynamic, with actuators bending flat mirrors into the elliptic shapes required by the experiment. Today, as a result of improved techniques for developing highly finished and perfect surfaces, ellipsoidal and paraboloidal mirrors can be manufactured to a high degree of perfection. Focusing down to 100 nm spot size is achievable with KB systems.

The reflecting multilayer supermirrors are able to focus X-rays over large energy range, whereas Bragg reflecting multilayer mirrors focus only a small energy bandwidth ($\sim$1–2%). As, within a given energy interval, the optical properties for total reflecting optics are independent of the X-ray wavelength, the focal spot is retained while tuning the energy. Therefore, experiments requiring energy tuning, like spectroscopy, can be performed without any readjustment of the optics. However, the disadvantage of grazing incidence optic is its inherent low acceptance and it is mostly used for scanning microscopes.

KB systems at the ESRF are based on dynamical bending systems where an initially flat, superpolished plate is used [13,19–21]. The obvious advantage of dynamical bending is that it permits one to tune the focusing conditions. Different mechanical benders are available at the ESRF. One can easily choose the most suitable system according to the experimental requirements, such as energy and energy range, the focusing parameters such as magnification and focusing distance. In addition, optimal substrate coatings, i.e., single layer mirrors or multilayers, can be used. The typical geometrical characteristics of the ESRF KB systems are focal distances ranging from 0.1 to 3 m and circular or elliptical bending radii varying from 20 to 1,000 m. Ideally KB systems require easy alignment procedure and they must preserve coherence or the wavefront of the reflected beam. Newly developed surface preparation techniques and a computer control alignment procedure allow a spot size of about 100×100 nm to be achieved. It is of great importance that the bending radii of the mirrors remain constant during several hours and even days of experimental measurements. Hence, the mirror mounting technique is a crucial point. Furthermore, vibrations should not deteriorate the spot by more than the mirror slope errors. At present, a typical value of the mirror local slope error corresponds to less than 0.3–0.4 μrad after polishing. To preserve high

reflectivity, a good level of vacuum is required to avoid surface contamination. Normally, a KB prealignment operation is employed, consisting of a laser self-alignment mirror setup inserted temporarily in front of the KB system. Final alignment is done with X-ray beam.

Most ESRF beamlines are equipped with in-house developed KB systems. More than 50 mirrors have been built and installed for microfocusing applications. Some of them are mounted in pairs to make up KB systems with different dynamical technologies. Many substrates are multilayer-coated according to energy, energy tunability, acceptance, and reflectivity requirements. The developed technology allows to achieve resolution below 100 nm, and 45 nm was measured recently at ID19 using 24 keV [13].

Although KB mirrors with benders enable the focal length to be varied, the benders are bulky and the stability achieved is not sufficient to support long-time scanning experiments on nanofocusing systems. The efficiency for microfocusing is affected by dynamic stability. In their actual usage of X-ray KB optics, the ease of setup is a very important factor. As was recognized at the other facilities, the procedures involved in mirror bending to form an exact ellipse from a flat surface are so complicated that a long time is needed to set up and optimize the system.

For these reasons static KB systems were chosen at the SPring-8 [12,22–28] and APS [29–35] facilities. For KB mirror fabrication at SPring-8, plasma chemical vaporization machining (PCVM) is employed for rough figuring, and elastic emission machining (EEM) is used for final figuring and surface super smoothing. These methods do not cause mechanical damage to the processed surfaces because their removal mechanism is based on chemical reactions. By combining these two methods, surfaces of unprecedented accuracy can be created with 0.1 nm controllability and 0.3 mm spatial resolution. To control the surface accuracy, the combined technique of microstitching interferometry and relative-angle-determinable stitching interferometry (RADSI) is used. This technique makes possible the measurement of elliptical surface profiles with a spatial resolution of 0.03 mm and measurement height accuracy close to 1 nm. Typically, after the final figuring the surfaces were coated by a 50 nm Pt layer using an electron evaporation method. The KB system was tested at the 1-km-long beamline BL29XUL at SPring-8 using a 15 keV monochromatic beam. A focal spot of 36 nm (horizontal) and 48 nm (vertical) was measured [12]. This proposed KB device employing precisely figured mirrors is promising, not only on the basis of focusing performances, but also as a user-friendly instrumentation.

Elliptical surfaces can be obtained by differentially coating a flat or a spherical mirror with a continuously variable amount of gold. This idea was proposed more than 60 years ago and was recently realized at the APS [29–35]. Profile coatings have been applied on both cylindrical and flat Si substrates to make the desired elliptical shape. In a profile-coating process, the sputter source power is kept constant, while the substrate is passed over a contoured mask at a constant speed to obtain the desired profile along the direction

perpendicular to the substrate-moving direction. A KB mirror pair, made using Au as the coating material, was recently tested at the APS, and X-ray results showed a focused spot size of $80 \times 70\,\mathrm{nm}^2$ [35].

Capillaries

Similar to reflective mirrors, monocapillary optics rely on total external reflection of the X-rays from the internal surface of the tube to transport X-rays. Typical glass materials that have been used to fabricate capillary optics are borosilicate, lead based, and silica glasses. For hard X-rays the typical values for critical angles are 0.1–10 mrad. The simplest form of a capillary is straight (cylindrical) glass tube; these have first been used in the 1950s to guide X-rays from the source point to a distant sample. This leads to an effective reduction of the source sample distance and thus to an increase in flux on the sample. The next step was to use tapered capillaries not only to guide but moreover to squeeze the X-rays to a very small spot [36, 37] (see Fig. 17.3a). The first experiments were performed with conventional X-ray tubes. In the late 1980s, conical tapered capillaries were tested at synchrotron facilities [14, 36–38].

Tapered capillaries were shown to have nanofocusing capabilities more than 10 years ago [14]. However, no appreciable progress of using such simple devices for nanobeams has been made since that time. For multibounce capillaries, the problems are well understood and consist of significant losses in the multireflection process and almost zero-working distance, which substantially limits practical applications of capillaries in X-ray microscopy. On the other hand, proposed single-bounce capillaries [39] show a great potential in developing nanofocusing devices (Fig. 17.3b). Parabolic and elliptical capillaries have a large focal distance and very high reflectivity [40–43]. In a typical process the predetermined capillary profile is achieved by "pulling" an originally straight uniform glass tube with accurate control of mechanical movements and heating parameters. Unfortunately, because of some unavoidable factors, i.e., surface slope errors of the original glass tube and nonuniform mechanical movement, it is difficult to reliably achieve elliptical or parabolic shapes with the desired low-figure errors. State-of-the-art technology allows one to produce a capillary with 70 μrad slope errors [41]. Obviously such slope errors limit the resolution of the optics to a size of about 10 μm.

To overcome these problems, the use of a small elliptical capillary made by a stationary pulling technique has been proposed, where the elliptical shape is
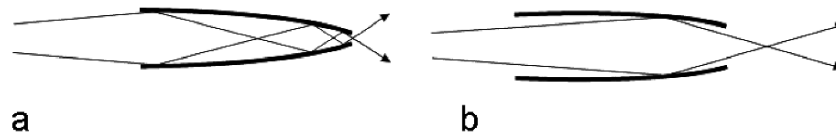

Fig. 17.3. Tapered multibounce (**a**) and single bounce (**b**) capillaries
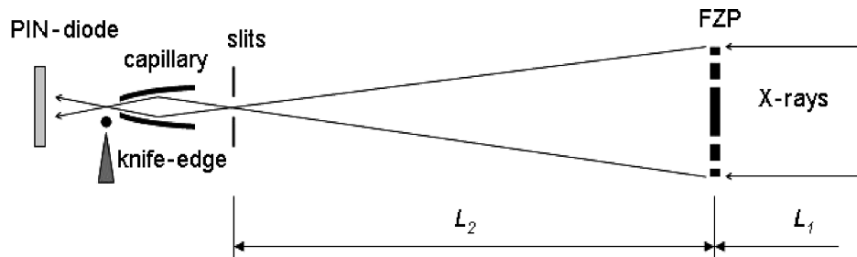
Fig. 17.4. Two-step focusing based on a Fresnel zone plate with a capillary

achieved by stretching an air bubble inside a glass fiber with constant velocity [44]. It appears that this approach might show a better quality surface as compared to the computer-controlled glass tube pulling process with a variable speed. For best performance of the ellipsoidal capillary a Fresnel zone plate was used to generate a secondary source at the first ellipse focus [15] (Fig. 17.4). The FZP serves as a first microfocusing element to produce a demagnified micrometer image of the source and then the elliptical capillary makes a final compression of the beam down to 250–500 nm. In general, the two-step focusing setup provides three important benefits: it significantly improves the flux by increasing the overall acceptance of the optical system; it makes possible optimal aberration-free focusing by the elliptical capillary surface; and it considerably minimizes the influence of slope errors. For practical applications, off-axis illumination of the capillary by a small prefocused beam eliminates the beam transmitted through the exit aperture and makes for an easy implementation of a beamstop. By accurate scanning of the tiny beam along the capillary surface one can control the demagnification factor and zoom the focal spot size.

The proposed approach allows one to shorten a small capillary further down to 5–10 mm, making it easy to align and operate. Use of short capillaries might open the possibility of coating the inside of capillaries with smooth films of the desirable materials such as platinum or gold. In this connection metal capillary optics look very attractive [45]. Finally, the single-bounce ellipsoidal capillaries are very attractive for X-ray nanobeam techniques because they are so simple and can potentially be reproduced inexpensively.

Waveguides

An X-ray planar waveguide is a thin film resonator in which a low absorbing material is enclosed between two metal layers with a smaller refractive index [46]. For particular grazing incidence angles, a resonator effect takes place inside the resonator film. Schematic representation of a thin-film waveguide is shown in Fig. 17.5. The beam is compressed in one direction and the trapped wave emerges from the end of the waveguide with enhanced intensity. In the direction of beam compression, the beam leaves the waveguide with the
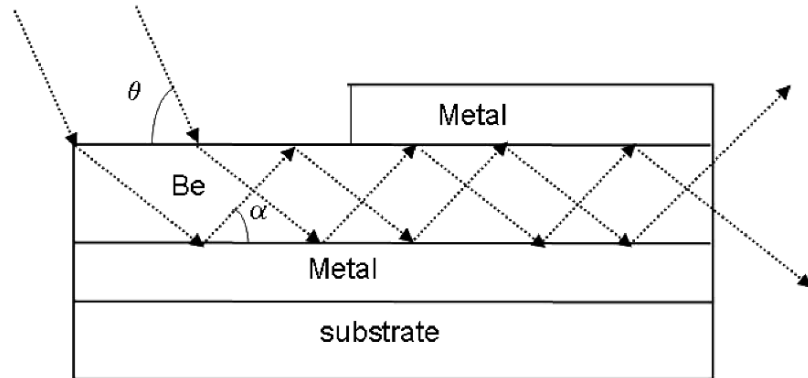
Fig. 17.5. The waveguide structure. θ is the incidence angle on the waveguide surface; incidence angle α on the interior metal surface of the waveguide differs from θ due to the refraction on the film

vertical size limited by the resonator layer thickness, which can be as small as 100 nm [47–49]. The cover layer and under layer can be constituted of the same material. To date, X-ray waveguide optics have been exclusively one-dimensional, whereas most nanobeam applications require two-dimensional point beams. Recently, the first proof of principle that resonant beam coupling can be realized in two dimensions was reported [16,50]. The hard X-ray beam with a cross section of $25 \times 47 \, \text{nm}^2$ (FWHM) is impressive. Nevertheless, many technological improvements will be required before this device can be used as an efficient X-ray point source.

17.3.2 Fresnel Zone Plates

The focusing properties of zone plates were first discussed in the latter part of the nineteenth century, and Baez originally suggested their use as X-ray optical elements in 1952 [51]. In their most common form, this is circular diffraction grating that works as a lens for monochromatic light. A Fresnel zone plate consists of a series of concentric rings of radius $r_n^2 = n\lambda F$. The rings become narrower with increase in radius until the last, narrowest zone of width Δr_n is reached (Fig. 17.6). Linear, square, and elliptical zone plates have also been considered, but only circular and, to a lesser extent, linear and elliptical forms have generally been used. The focusing capability is based on constructive interference of the wavefront modified by passage through the zone plate. The wavefront modification is obtained through the introduction of a relative change in amplitude or phase in the beams emerging from two neighboring zones. A zone plate is called an amplitude zone plate if the focusing results from different absorptions between two neighboring zones. It is called a phase zone plate if the phase change upon transmission through a zone is the mechanism for focusing.
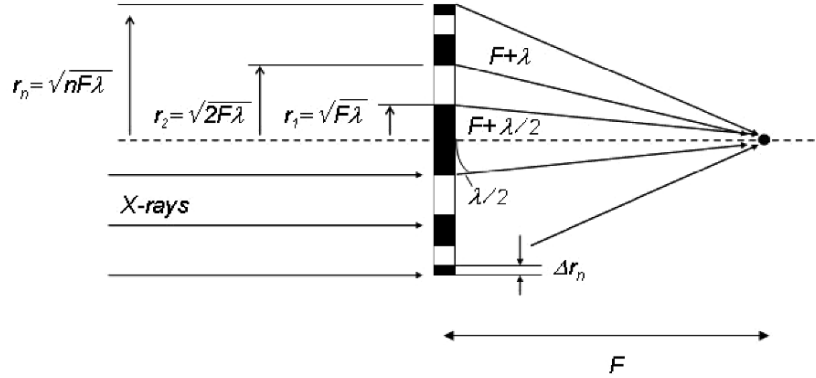
Fig. 17.6. Fresnel zone plate geometry

Just as the Rayleigh resolution of a light microscope lens is determined by its numerical aperture (NA), the Rayleigh resolution of a zone plate is determined by its maximum diffraction angle $NA = \lambda/(2\Delta r_n)$, so that the Rayleigh resolution is $1.22\Delta r_n$. Using the state-of-the-art lithographic technologies, zone plates with an outermost ring width of less than $20\,nm$ can be fabricated. If illuminated with an X-ray beam whose spatial coherence length is equal to or greater than the diameter of the zone plate, a diffraction-limited focus can be obtained. The efficiency of zone plates, i.e., the fraction of the incident photons diffracted into the focal spot, depends on the phase shift and attenuation introduced by the FZP structures. In the soft X-ray region, zone plate efficiency is limited to about 15% due to photoelectric absorption. For X-ray energies greater than $4\,keV$, it is in principle possible to produce phase zone plates with focusing efficiencies close to 40%.

The efficiency of a binary FZP reaches its maximum value when the structure height is chosen to introduce a phase shift of π. As a phase shift generally decreases with increase in photon energy, higher and higher structures are required to provide useful efficiency values for harder X-rays. For example, the appropriate zone thickness for $10\,keV$ X-rays is estimated to be about $2\,\mu m$ even for high density materials like gold or tantalum. The resulting extreme aspect ratios (height/width of finest zone) are the reason why FZPs for hard X-rays cannot be made with a zone width as small as the ones for soft X-rays. In fact, FZPs have only very rarely been used for energies beyond $12\,keV$. It should be noted that APS [17, 52–68] and SPring-8 [69–87] have very strong in-house FZP long-term development programs for hard X-ray applications. Metal based FZPs are now commercially available from X-Radia (USA) [88] and NTT (Japan) [89].

As mentioned earlier, the spatial resolution of a zone plate is determined by the outermost zone width, Δr_n. Hence, manufacturing techniques must be capable of delivering small line widths over large areas, to give apertures as large as possible, with zone thicknesses of correct values to give good

diffraction efficiencies. The accuracy of the technique must be sufficient to yield zone boundaries within about one-third of the outer zone width. To date, basically two main approaches are used to achieve this. The mostly used technique for FZP manufacturing is based on semiconductor MEMS (micro-electro-mechanical systems) technology, which is similar to the technique employed in the manufacture of microcircuits. This technique is based on lithography methods with consecutive deep pattern transfer. Since optical lithography is limited to $0.2\,\mu m$ resolution, mainly electron beam lithography is used for manufacturing high resolution zone plates. Currently, the best performing zone plate lenses for multi-kiloelectronvolt X-rays in terms of resolution and efficiency are fabricated by means of a deep pattern transfer process.

To reproduce the zone plate structure in a suitable material the lithographically based techniques can be subdivided into two main transfer methods: (a) wet or reactive ion etching and (b) electrochemical deposition (electroplating). The first method can be applied to metals and semiconductors and is used for example by NTT in Japan (Ta FZP) [72–76, 81, 84–86] and by PSI (Si FZP) [90–94]. Electroplating can be applied only for metals and typically uses gold and nickel [88, 95–99]. To date, typical aspect ratios achieved using e-beam lithography and consecutive pattern transfer for $100\,nm$ structures are of the order of 10:1–15:1: for wet etching Si – 15:1 [100]; for reactive ion etching Ni, W – 10:1 [89]; for electroplating, Au – 16:1 [88].

Recently, microfabrication MEMS technology was successfully used to produce Si-FZP for hard X-rays, and using reactive ion etching of Si an aspect-ratio of 40–50 has been demonstrated for modest resolution zone plates with a $400\,nm$ outermost zone [101, 102]. Compared to other materials commonly used for FZPs (Ni, Ta, Au), the absorption losses are negligible in Si. The phase shifting property of Si is also comparatively weak. The structure height required for optimum efficiency at $24\,keV$, for example, is almost $30\,\mu m$ (Fig. 17.7). The advantage of Si MEMS technology is that Si chips with a number of different diffraction optical elements (DOE-chips) can be made. At ESRF, three types of DOE-chips are used by different beamlines as medium and long focal distance optics (see Table 17.3).

To overcome the aspect ratio limitation inherent in the lithography technique, the sputtered-sliced FZP (ss-FZP) method was proposed in 1982 [103]. In this technique, two different materials of heavy and light elements are alternately deposited on a rotating gold wire core to give a concentric multilayer structure. The ss-FZP is then produced from the multilayer wire sample by making slices perpendicular to the wire axis and then thinning and polishing the slice down to the required thickness (10–200 μm). It has been found that for these ss-FZPs, imperfections in the wire and defects during deposition lead to accumulative errors in the fine outermost zones, which are deposited last. Furthermore, it proved very difficult to slice the wire without deforming the delicate zone plate structure. In principle, this method is capable of producing zone plates with 10–50 nm resolution, and strong activity is
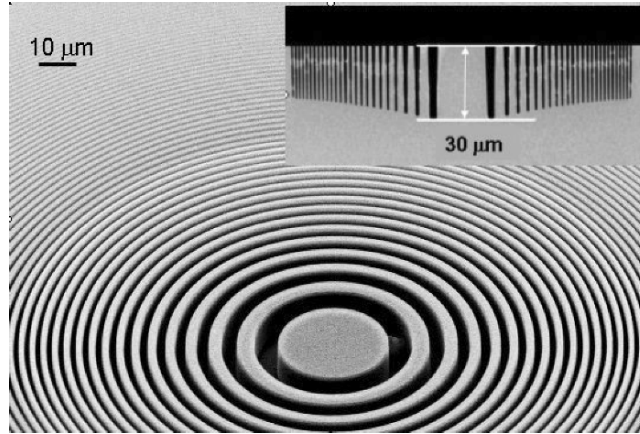
Fig. 17.7. SEM image of the SI Fresnel zone plate. Insert shows the cross section of FZP Chip 3 optimized for 23 keV (see Table 4.1.3)

Table 17.3. Chip specification

	T_{m}/h (µm)	E_{range} (keV)	η_{max} (%)	E_{max} (keV)
Chip1	12/9	6–12	30	7.5
Chip2	80/16	11–21	26	14
Chip3	90/30	17–40	32	23

T_{m}, thickness of silicon membrane; h, maximum height of the zone phase profile; E_{range}, energy range with focusing efficiency higher than 20%; η_{max}, maximum focusing efficiency (achieved at energy E_{max}); E_{max}, energy at which maximum efficiency η_{max} is achieved

going on at SPring-8 in collaboration with the Photonic Research Institute AIST (Osaka) [77–79, 85].

Another way of solving the aspect-ratio problem proposed recently by a PSI group is to apply an inclined geometry for a linear zone plate. Linear Si lenses were produced by electron-beam lithography and anisotropic wet etching. Two linear FZPs in a crossed geometry similar to a KB mirror system allowed one to produce a focal spot of 170 nm at 12.7 keV [100]. In addition, the device, consisting of two crossed linear lenses, can be matched with the asymmetric shape of synchrotron X-ray sources. This results in a better performance in terms of focal spot shape, spot size, and flux within the spot. Obviously, using two linear zone plates in series has the disadvantage that the losses in two optical components have to be considered.

It should be noted that achieving the utmost resolution is much easier in a magnified imaging mode as compared with a microbeam or microprobe mode. The microbeam size is a result of the convolution of the demagnified source size and the resolution of the optics, whereas in the imaging mode the

source size is not important and the resolution of the image depends only on the intrinsic resolution of the optical element. As a most illustrative example, a 60 nm resolution has been obtained using a laboratory source with 5.4 keV X-rays by an X-Radia full-field microscope equipped with Au FZPs [104].

It is clear, however, that the focusing properties of all binary FZPs developed for X-ray applications are far weaker than those of an ideal lens because a significant fraction of incident photons is delivered to the undiffracted zero-order beam and to diffraction orders other than the primary, first order. For instance, although in principle the undiffracted zero-order beam for an ideal phase zone plate is completely reduced to zero, about 60% of the incident beam is still delivered to other unwanted orders. Improving the focusing efficiency of a zone plate in the X-ray spectral region by optimizing the zone profiles was studied in detail in a theoretical article by Tatchyn in 1990 [105], and the first zone plate with a blazed zone profile was manufactured at Wisconsin and tested at the APS using 8 keV X-rays showing 45% efficiency for linear and 39% efficiency for circular ZPs, respectively [57]. Later 55% efficiency for the nickel circular zone plate at 7 keV was achieved at the ESRF [95]. This measured focusing efficiency is the highest value that has been demonstrated in the X-ray region for zone plate optics. In practice, the production of high-resolution zone plates with a blazed profile is very complicated and expensive and a resolution better than 0.5 μm was never realized for these devices.

A novel approach for high-resolution X-ray focusing, a Multilayer Laue Lens (MLL), was proposed at the APS [17, 62, 63, 68]. The MLL concept is a system of two crossed linear zone plates, manufactured by deposition techniques. The approach involves the deposition of a multilayer with a graded period, sectioning it to the appropriate thickness, assembling the sections at the optimum angle, and using it in Laue geometry for focusing. The approach is particularly well suited for high-resolution focusing optics for use at high photon energies (30 nm resolution and 70% efficiency).

To overcome the aspect-ratio limitation to produce thicker FZPs, one can attempt a multiple zone plate setup. Two stacked zone plates made of gold were tested at 50 keV [59, 60], but did not show the theoretically predicted efficiency and resolution for the following reasons: the zone plates were not exactly identical; the alignment procedure was not accurate enough; the stability was not sufficient; and a 3 mm separation of zone plates was far more than that is allowable.

Recently, the Microoptics test bench at BM5 at the ESRF was used for the FZP stacking technique, using Si FZP chips described earlier [101, 102]. The first FZP chip was mounted on the optics stage with all necessary angular and linear movements. The second chip was mounted on the slit support frame with two X-Y linear translations. The precise and smooth vertical movement of the Microoptics test bench enabled one to check the alignment of different FZPs on the chip. Achieving the exactly aligned condition was easily done by a straightforward X-ray phase contrast imaging technique by looking at the X-ray CCD camera image of the beam. When you look through one FZP at
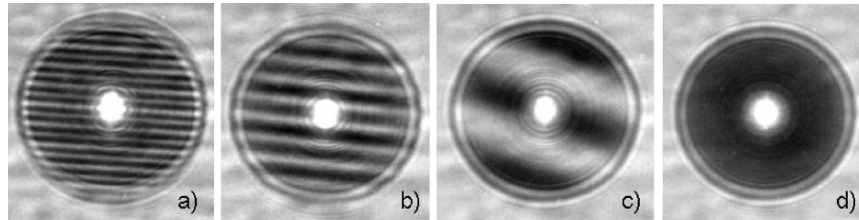
Fig. 17.8. Experimental moiré patterns recorded at 12 keV at 76 cm, with 6 μm (**a**), 3 μm (**b**), 1 μm (**c**), and 0 μm (**d**) lateral displacement

another, a *moiré pattern* always appears as the two repetitive patterns overlap. A slight motion of one of the objects creates large-scale changes in the moiré pattern (Fig. 17.8). Two chips with zone plates were joined together in a way that the front side of the first chip faces the backside of the other one. Therefore, the corresponding zone plates are separated from each other by a substrate thickness of 500 μm. For two zone plates to behave as one, their relative transverse positions must be adjusted properly to within a hundred nanometers, so as to directly line up the zones of the two elements. A compact micromechanical motion system (piezo-based Y-Z stage) was used to execute such precise alignment with 50 nm step size. When two zone plates are nearly perfectly aligned, the image shows no interference fringe patterns – the fringe spacing becoming infinite as the stacking alignment becomes perfect. To provide the desired stability, zone plates are bonded together with epoxy glue with slow solidification speed for the on-line alignment correction.

Two identical Si Chips3 were used for stacking in order to focus 50 keV X-rays. Each chip contains nine different FZP elements (five circular and four linear) with a depth of 30 μm, providing a focusing efficiency of about 34% at 23 keV. Two closely juxtaposed zone plates focus 50 keV X-rays with 35% efficiency [100–102]. Thus, there is a significant improvement in going from one to two such elements. It should be noted that such systems provide a focused beam with more than 20% efficiency in the energy range from 40 to 100 keV and can be used now for microdiffraction/scattering experiments. One can envisage some new imaging and interferometry techniques using FZP systems at higher energies. The technique developed will be used for future Fresnel optics with higher resolution and can be extended to "thin" nanofocusing FZPs.

17.3.3 Refractive Optics

Refractive lenses made of glass are among the most widely used optical components for visible light, with the wide spectrum of applications in focusing and imaging. Refractive lenses for X-rays were considered unfeasible for a long time due to the weak refraction and strong absorption. However, in 1996 it
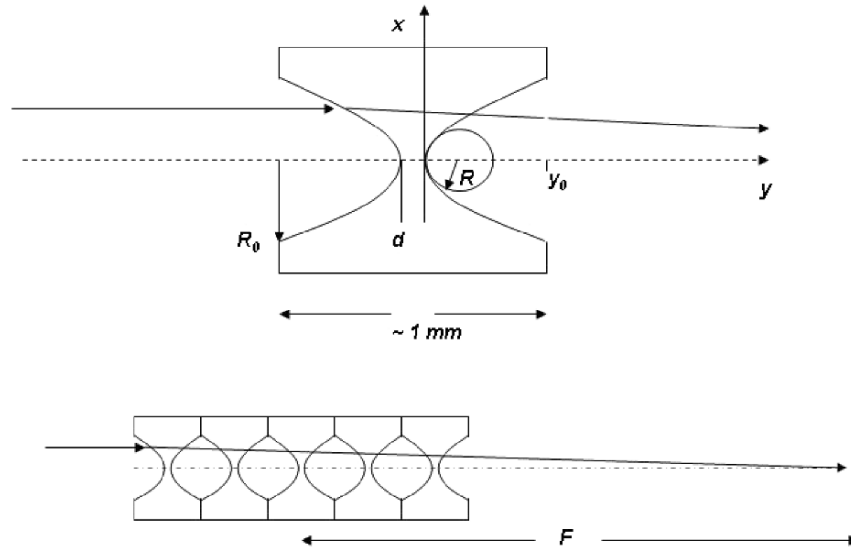
Fig. 17.9. Parabolic compound refractive lens (CRL). The individual lenses (**a**) and stacked behind one another to form a CRL

was shown that focusing by X-ray lenses is possible [106]. Since the $(1 - \delta)$ in the index of refraction is smaller than 1, lenses must have a concave shape [106–108]. To obtain a focal length F in the range of 1 m, many single lenses have to be stacked behind each other to form a compound refractive lens (CRL) as shown in Fig. 17.9. Fabricating the lenses from low-Z materials like Li, Be, B, C, and Al minimizes the problems associated with absorption. The focal length of such CRL with a parabolic profile $x^2 = 2Ry$ and N individual biconcave lenses is $F = R/2N\delta$, where R is the radius of curvature at the apex of parabola. A lens with thickness $2y_0 + d$ has an aperture $2R_0 = 2\sqrt{2Ry_0}$.

Refractive lenses act as a conventional lens and one can apply the Gauss lens formula, which relates the source distance p, the image distance q, and the focal distance F via $q = Fp\,(p - F)$. The diffraction-limited resolution of the lens Δ is defined by an effective aperture: $\Delta = 0.75\lambda/2\mathrm{NA}$, where the numerical aperture is $\mathrm{NA} = A_{\mathrm{eff}}/2q$. A_{eff} is the effective aperture of the lens, reduced by photon absorption and scattering, compared with the geometrical aperture $2R_0$.

The first lenses consisted of a row of holes, about 1 mm in diameter, drilled in a material such as Al or Be [107]. Two of these lenses in crossed geometry are able to focus an X-ray beam to a spot size of a few microns. Soon after this first successful experimental demonstration it was understood that refractive lenses can be used as a condensers or collimators with relatively long focal distances. Be, Graphite, and Al lenses were installed at the front-ends (FE) about 24 m from the source at various beamlines [109–112]. The typical FE

Table 17.4. Typical parameters of the FE CRL lenses at the ESRF

Lens	N	E for $L_2 = 41$ m (keV)	E for collimation (keV)	f for $E = 20$ keV (m)
1	7	12.7	15.1	42
2	16	17.0	22.9	18.4
3	28	22.8	30.2	10.5
4	44	28.2	37.9	6.7
5	64	35	45.7	4.6

CRL consists of a series of cylindrical holes drilled into a material. By varying the number of holes and their radius, it is possible to fine-tune the focal length of the lenses, making them a very useful device not only to focus but also to collimate a divergent X-ray beam: by choosing $F = p$ one obtains $q = \infty$, and the beam after the lens will be parallel [113–115].

Table 17.4 gives an overview for typical focal lengths of the FE lenses, collimation energies, and energies used to image the source size with a camera in the second experimental hutch.

Nowadays some ESRF beamlines (ID2, ID16, and ID18) are equipped with cylindrical CRL installed in optics hutches. For example, at ID18, in addition to FE lenses there is a CRL with 120 Al holes installed up-stream of the high-heatload (HHL) monochromator at ID18 to meet the acceptance of the Si (111) reflection for energies above 30 keV. At 64 keV this lens collimates the beam from 15 to 1.5 μrad and improves the resolution from about 10–1 eV while keeping the integral flux. Down-stream of the HHL monochromator another CRL is also installed to match the beam divergence to the acceptance of the first crystal of the high resolution monochromator. At 14.4 keV the intrinsic divergence of the X-ray beam of about 20 μrad has been decreased to 6 μrad, improving the throughput by a factor of two and the resolution from 0.82 to 0.65 meV [113].

In the meantime, Al and Be parabolic refractive lenses have been developed in collaboration with Aachen University [116–124]. They focus in both directions and are free of spherical aberrations and other distortions. Parabolic refractive lenses can be used to focus hard X-rays in both directions in the range from about 5 keV to about 200 keV. They are compact, robust, and easy to align and to operate. They can be used like glass lenses used for visible light and provide a resolution on the order of 300–500 nm, the main difference being that numerical aperture is much smaller than 1 [116]. Their main applications are in micro- and nanofocusing and in imaging by absorption and phase contrast [121]. In combination with tomography, 3D imaging of opaque media with sub-micrometer resolution is possible [123]. The Be and Al lenses for two-dimensional focusing are now used extensively as a standard tool in experiments. Table 17.5 shows the ESRF beamlines equipped by Al and Be parabolic refractive lenses made by RWTH in Aachen.

Table 17.5. Parabolic CRLs from RWTH Aachen used at the ESRF beamlines

Beam line	Material	Energy (keV)	Number of indiv. lenses	Source distance (m)	Focal distance (m)
ID1	Be	6–9	20	42	0.5–1.5
ID10A	Be	6–20	20	40/55	0.5–3
ID10B	Be	7–20	40	35/40	0.5–3
ID11	Be	15–80	61	30/55	1–10
	Al	20–100	254	55/100	0.5–10
ID11/ID15	Al	20–200	500	40/50/60	0.5–10
ID13	Be	12–14	24	1.5	1.5
ID22	Al	6–10	200	40/50	0.5–1
	Be	8–60	100	40/50	10–30
ID18F	Al	15–30	200	20	20
ID32	Be	8–23	15	34	6–13
ID14	Be	14	30	40	0.5–1.5
MOTB/BM5	Be	7–30	25	40/54	1
	Al	15–60	200	40/54	0.5–50
MPI/ID15	Al	50–90	300	60	3–6

In recent years a significant demand for focusing of hard X-rays above 40 keV has developed. A number of new applications such as surface and interface scattering, high pressure Compton magnetic scattering, and depth strain analysis using powder microdiffraction are under extensive development [125–127]. The Max–Planck Institute (MPI) end-station for surface and interface scattering, which has been recently installed at ID15, is a nice example of such a development.

Recently, microelectronics planar fabrication technology has been applied to create silicon-based devices [128–135]. One-dimensionally focusing parabolic refractive lenses have been manufactured in collaboration with the Institute of Microelectronics Technology (Chernogolovka, Russia) and Dortmund University using lithography and highly anisotropic plasma etching techniques. This type of planar lens is well suited for high-resolution diffraction experiments, including standing wave techniques [133–135]. It is possible to make a composite lens consisting of a set of parallel parabolas with different focal distances. To change the focal distance or the desirable working energy, one can switch from one array to another by moving the composite lens. Driven by the requirements of new 100-m-long beamlines at the ESRF, Si planar parabolic lenses were designed and fabricated (Fig. 17.10). They have a short focal distance in the energy range of 10 and 100 keV. The optical test of the new planar lenses was performed at the ESRF beamlines BM5 and ID15. The resolution below 200 nm was measured in the energy region of 15–80 keV. The best resolution of 150 nm was demonstrated at 50 keV energy. Using the same approach
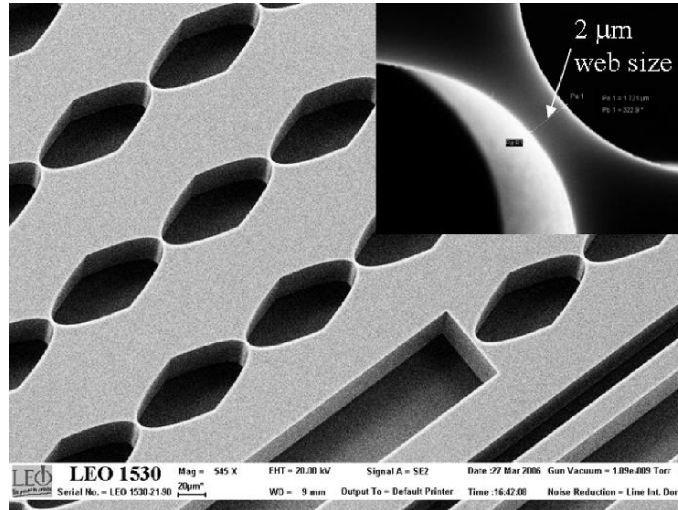
Fig. 17.10. SEM image of a Si planar refractive lens. The insert shows the 2 µm web size

of the Si-planar technology, nanofocusing lenses were developed by the Aachen group [136–138]. They have a focal distance in the range of a few millimeters at hard X-ray energies. In a crossed geometry, two lenses were used at ID13 to generate a nanobeam with a lateral size of 115 nm by 160 nm at 15.2 keV, and in December 2004 a focus spot of about 50 nm was achieved [18]. The planar lens technology is being transferred to materials like diamond that has low X-ray absorption, low thermal expansion, and high heat conductivity [139,140]. These lenses are mechanically robust and can withstand the high heat load of the white beam produced by the ESRF in vacuum undulators and from future X-ray free electron lasers.

The applicability of Al lenses for microbeam analysis at energies above 100 keV is limited by the physical size of the lens assembly, because the number of individual lenses required to produce a reasonable focal distance grows quickly with energy. Using denser lens materials, such as nickel, the number of lenses that are needed can be drastically reduced. While the absorption in nickel is still tolerable, its density and thus its refraction are higher compared to the low Z materials used. Nickel is the most promising since it is radiation and corrosion stable and, what is more important, it is one of the best materials for electroplating. LIGA technology including deep X-ray lithography and electroplating has been widely used in the last ten years for the fabrication of various microstructures in Ni. These techniques make possible the formation of planar lens arrays with a wide range of parameters. Lens apertures can range from a few microns to a few millimeters. Structures up to few millimeters in depth can be realized. Their focal distances can range from a few
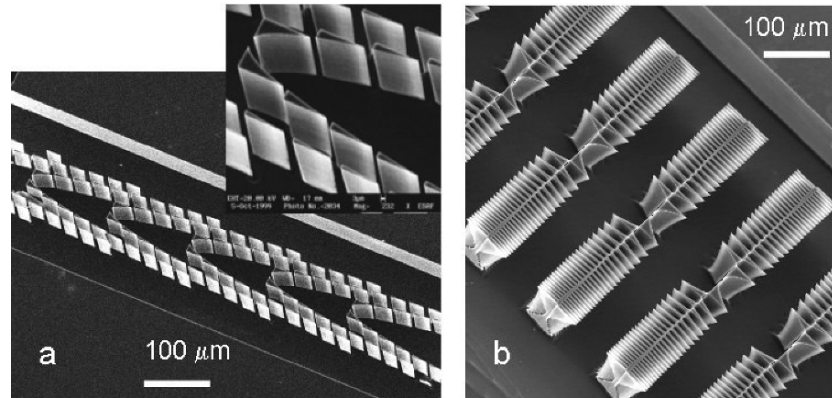
Fig. 17.11. SEM images of two different types of kinoform lenses made in Si (see text) [128] (**a**); [130] (**b**)

millimeters to tens of meters. Ni planar refractive lenses have been manufactured by deep X-ray lithography and LIGA techniques. The optical properties of lenses were determined at the ESRF ID15 beamline at energies from 40 to 220 keV. One- and two-dimensional focusing was performed. Sub-micrometer focusing was measured in the energy range from 40 to 150 keV [141, 142].

Recently, holographic or kinoform optical elements (Fig. 17.11) with a combination of refractive and diffractive properties were manufactured [128, 130]. In these refractive lenses passive parts of the material that cause multiples of 2π in phase shift are removed thereby reducing absorption. With this method drawbacks of purely diffractive or refractive elements are eliminated and advantages such as high transmission, absence of zero-order, high efficiency are combined. Recently, Ni kinoform lenses made by LIGA focused 212 keV X-rays to a focal line 5 μm wide with a tenfold gain [141, 142]. The ability to manipulate the local amplitude and phase of the incoming wave opens the perspective to make a new class of beamshaping X-ray optics for coherent synchrotron radiation.

17.4 Concluding Remarks

The foregoing overview shows the tremendous development in the possibilities for X-ray focusing that now makes possible the construction of powerful instruments for microscopy at synchrotron radiation beamlines.

In conclusion we compare the different focusing systems. First, we should mention that reflective, diffractive, and refractive microoptics have the following features in common:

– All three types are under intensive development at all three big hard X-ray facilities
– They are becoming commercially available
– They are used as a standard instrumentation at the beamlines
– All three types show nanofocusing capabilities

KB mirrors have an intrinsic advantage over the other focusing elements, such as Fresnel zone plates and refractive optics: nondispersive or broadband focusing. In the case of dynamic KB systems sophisticated bending techniques have been developed to bend mirrors to the desired elliptical shape for micro- and nanofocusing. The vibration level has to be controlled to within a few microradians and the figure accuracy of the elliptical mirrors to within a few nanometers. This is technologically challenging. The reflected beam is deflected with respect to the incoming beam. These constraints can all be managed, but have to be taken into account when selecting the most appropriate microfocusing technology. Mirrors with benders can provide an adjustable focal length, but the benders are bulky. Monolithic or static KB systems are much easier to use if the desired elliptical surface profile can be fabricated.

FZP and refractive optics being in-line optics have certain advantages over KB systems:

– On-axis optics do not change the beam direction
– They provide easy alignment and operation
– They can be easily implemented at any beamline (including nonspecific beamlines)
– In the case of nanofocusing geometries FZP and CRL should have greater distance from the optics to the sample

FZP elements have attractive features in that they are very compact and easy to use. The alignment mechanics requires basically only two orthogonal translations (XZ) and therefore they can be easily used at any nonspecific beamline [143, 144]. Si FZPs are compatible with ML and "pink" beams because of high radiation and temperature stability.

The advantages of CRLs are the following: they are very robust and small, the focal length and size are adjustable by adding or removing individual lenses, and the lenses can withstand a high heatload. The lens aperture can range from a few microns to a few millimeters. Their focal distance can range from a few millimeters to tens of meters. What is more, CRLs can cover the energy range from 4 to 200 keV and higher.

Compared to mirrors, refractive lenses are about a factor of 1,000 less sensitive to surface roughness. This is an important aspect in the production process of the lenses. Surface roughness plays no role in imaging by refractive X-ray lenses.

For comparing different optics, it is important to consider the physical limits to the efficient focusing of hard X-rays. It was found that mirrors

and waveguides have a numerical aperture, which is limited by the critical angle of total reflection. The ultimate resolution limit is 10 nm [145], while for refractive optics this limit is slightly lower and 2 nm may be achievable [146]. Unlike reflective and refractive optics, zone plates can focus X-rays below 1 nm [147, 148]. In this case, complex multilayer zone plates have to be manufactured and Bragg conditions have to be fulfilled for the outermost zones. As for conventional zone plates, there is a simple pathway to achieve sub-10 nm resolution X-ray imaging by using a higher diffraction order, such as the third diffraction order of a currently available zone plate. While progress in the fabrication of hard X-ray zone plates has significantly advanced within the last few years, the pattern transfer fabrication process may reach a practical limit very soon. As the polymer structures of the electroplating mold become smaller and smaller in width they lose strength and tend to collapse during the fabrication process. Also, the directionality of the reactive ion etch may impose practical limits to the achievable sidewall angle in the resist, limiting the achievable width of features that can be fabricated. From current fabrication data it can be estimated that the practical limit for hard X-ray zone plates using current pattern transfer technology is 20–30 nm (structures height $\cong 1\,\mu$m). It is believed that by using higher diffraction orders, such as the third diffraction order, it would be possible to achieve sub-10 nm resolution X-ray imaging.

To discuss the applicability of one or another type of focusing systems for nanofocusing applications, let us consider the conditions for new 100-m-long beamlines at the ESRF. To obtain a resolution about 50 nm in the vertical direction we need to apply a demagnification factor of $\times 1{,}000$ for the vertical source size of 50 μm. Therefore, a microoptics device placed at the source-to-optics distance $p = 100$ m must have a focal length (distance to detector/sample distance) $q = 0.1$ m. We consider the following three optical systems:

– KB mirror system (Pt coated) with 40-mm-long mirrors and 30 mm working distance
– Fresnel zone plates with the outermost zone width 40 nm
– Planar refractive lenses made of Si, Be, and C (diamond)

The graph in Fig. 17.12 shows effective apertures or acceptances of the KB-mirrors, FZP and CRLs. The FZP effective aperture in the graph is normalized to the FZP efficiency ε: $A_{\mathrm{eff}} = A_{\mathrm{fzp}}\varepsilon$. We optimistically assume that the FZP is made with optimal thickness providing a phase shift π and an efficiency not less than 30% over the entire energy range. As can be seen from this graph, the FZP elements can be applied up to 20 keV energy, whereas KB-mirror systems look competitive up to 40–50 keV. Si nanofocusing lenses can easily beat FZP after 20–25 keV and become competitive with KB-m after 40 keV.

Use of microoptics and exploiting the high brilliance and the spatial coherence of the X-ray beam provided by the third generation synchrotron radiation
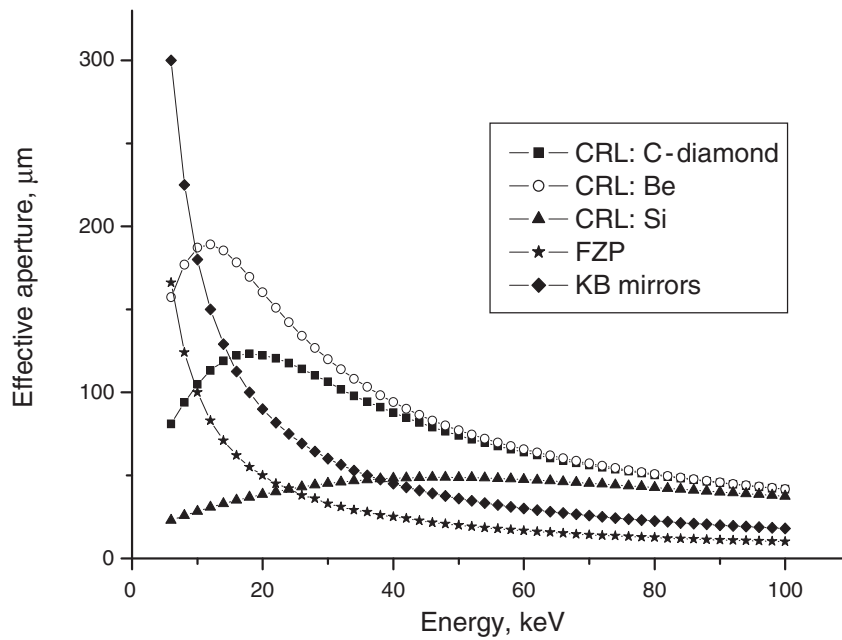
Fig. 17.12. Graph showing the effective aperture dependence vs. energy for different optical elements

sources makes possible high energy X-ray microscopy as a combination of diffraction, fluorescence, and imaging techniques. The availability of these techniques is opening up research opportunities for a broad range of disciplines, including material science, biology, environmental, and geosciences.

References

1. P. Goby, Comptes Rendue de l'Academie des Sciences Paris **156**, 686 (1913)
2. P. Kirkpatrick, A.V. Baez, J. Opt. Soc. Am. **38**, 766 (1948)
3. V.E. Cosslett, W.C. Nixon, Nature **168**, 24 (1951)
4. B. Niemann, D. Rudolph, G. Schmahl, Opt. Commun. **12**, 160 (1974)
5. J. Kirz, H. Rarback, Rev. Sci. Instrum. **56**, 1 (1985)
6. W. Chao, B.D. Harteneck, J.A. Liddle, E.H. Andersen, D.T. Attwood, Nature **435**, 1210 (2005)
7. A.G. Michette, *Optical Systems for Soft X-rays* (Plenum Press, New York, 1986)
8. A. Michette, S. Pfauntsch (eds.), *X-rays: The First Hundred Years* (Wiley, New York, 1997)
9. J. Thieme, G. Schmahl, D. Rudolph, E. Umbach (eds.), in *X-ray Microscopy and Spectroscopy*. Status Report from the Fifth International Conference, Wurzburg, August 19–23, 1996 (Springer-Verlag, Berlin Heidelberg, New York, 1998)

10. W. Meyer-Ilse, T. Warwick, D. Attwood (eds.), in *X-ray Microscopy Proceedings of the Sixth International Conference*, Berkeley, CA 1999. AIP Conference Proceedings 507 (American Institute of Physics, Melville, New York, 2000)

11. J. Susini, D. Joyeux, F. Polack (eds.), *X-ray Microscopy 2002, 7th International Conference on X-ray microscopy, ESRF*, Grenoble, France, July 28–August 2, 2002. EDP Sciences, Journal de Physique IV, vol. 104 (2003)

12. H. Mimura, S. Matsuyama, H. Yumoto, H. Hara, K. Yamamura, Y. Sano, M. Shibahara, K. Endo, Y. Mori, Y. Nishino, K. Tamasku, M. Yabashi, T. Ishikawa, K. Yamauchi, Jpn. J. Appl. Phys. **44**, L539 (2005)

13. O. Hignette, P. Cloetens, C. Morawe, C. Borel, W. Ludwig, P. Bernard, A. Rommeveaux, S. Bohic, AIP Conf. Proc. **879**, 792 (2007)

14. D.H. Bilderback, S.A. Hoffman, D.J. Thiel, Science **263**, 201 (1994)

15. A. Snigirev, A. Bjeoumikhov, A. Erko, I. Snigireva, M. Grigoriev, M. Erko, S. Bjeoumikhova, J. Synchrotron Radiat. **14**, 227 (2007)

16. A. Jarre, C. Fuhse, C. Ollinger, J. Seeger, R. Tucoulou, T. Salditt, Phys. Rev. Lett. **94**, 074801 (2005)

17. H.C. Kang, J. Maser, G.B. Stephenson, C. Liu, R. Conley, A.T. Macrander, S. Vogt, Phys. Rev. Lett. **96**, 127401 (2006)

18. C.G. Schroer, O. Kurapova, J. Patommel, P. Boye, J. Feldkamp, B. Lengeler, M. Burghammer, C. Riekel, L. Vincze, A. van der Hart, M. Kuchler, Appl. Phys. Lett. **87**, 124103 (2005)

19. Y. Dabin, G. Rostaing, O. Hignette, A. Rommeveaux, A. Freund, Proc. SPIE **4782**, 235 (2002)

20. O. Hignette, P. Cloetens, W.K. Lee, W. Ludwig, G. Rostaing, J. Phys. IY France **104**, 231 (2003)

21. O. Hignette, P. Cloetens, G. Rostaing, P. Bernard, C. Morawe, Rev. Sci. Instrum. **76**, 063709 (2005)

22. Y. Mori, K. Yamauchi, H. Mimura, Y. Sano, A. Saito, K. Ueno, K. Endo, A. Souvorov, M. Yabashi, K. Tamasaku, T. Ishikawa, Proc. SPIE **4782**, 58 (2002)

23. K. Yamauchi, K. Yamamura, H. Mimura, Y. Sano, A. Saito, A. Souvorov, M. Yabashi, K. Tamasaku, T. Ishikawa, Y. Mori, J. Synchrotron Radiat. **9**, 313 (2002)

24. K. Yamauchi, K. Yamamura, H. Mimura, Y. Sano, A. Saito, K. Endo, A. Souvorov, M. Yabashi, K. Tamasaku, T. Ishikawa, Y. Mori, Jpn. J. Appl. Phys. **42**, 7129 (2003)

25. K. Yamamura, K. Yamauchi, H. Mimura, Y. Sano, A. Saito, K. Endo, A. Souvorov, M. Yabashi, K. Tamasaku, T. Ishikawa, Y. Mori, Rev. Sci. Instrum. **74**, 4549 (2003)

26. H. Yumoto, H. Mimura, S. Matsuyama, H. Hara, K. Yamamura, Y. Sano, K. Ueno, K. Endo, Y. Mori, M. Yabashi, Y. Nishino, K. Tamasaku, T. Ishikawa, K. Yamauchi, Rev. Sci. Instrum. **76**, 063708 (2005)

27. S. Matsuyama, H. Mimura, H. Yumoto, K. Yamamura, Y. Sano, K. Endo, Y. Mori, Y. Nishino, K. Tamasku, T. Ishikawa, M. Yabashi, K. Yamauchi, Rev. Sci. Instrum. **76**, 083114 (2005)

28. H. Yumoto, H. Mimura, S. Matsuyama, S. Handa, Y. Sano, M. Yabashi, Y. Nishino, K. Tamasaku, T. Ishikawa, K. Yamauchi, Rev. Sci. Instrum. **77**, 063712 (2006)

29. G.E. Ice, J.S. Chung, J. Tischler, A. Lunt, L. Assoufid, Rev. Sci. Instrum. **71**, 2635 (2000)

30. A. Khounsary, G. Ice, P. Eng, Proc. SPIE **4782**, 65 (2002)
31. C. Liu, L. Assoufid, A.T. Macrander, G.E. Ice, J.Z. Tischler, Proc. SPIE **4782**, 104 (2002)
32. C. Liu, L. Assoufid, R. Conley, A.T. Macrander, G.E. Ice, J.Z. Tischler, Opt. Eng. **42**, 3622 (2003)
33. C. Liu, R. Conley, L. Assoufid, Z. Cai, J. Qian, A.T. Macrander, AIP Conf. Proc. **705**, 704 (2004)
34. G.E. Ice, E.D. Specht, J.Z. Tischler, A.M. Khounsary, L. Assoufid, C. Liu, Proc. SPIE **5347**, 1 (2005)
35. W. Liu, G.E. Ice, Z. Tischler, A. Khonsary, C. Liu, L. Assoufid, A.T. Macrander, Rev. Sci. Instrum. **76**, 113701 (2005)
36. D.R. Kreger, Recl. trav. Bot. Neerlandais **41**, 603 (1948)
37. E.A. Stern, Z. Kalman, A. Lewis, K. Lieberman, Appl. Opt. **27**, 5135 (1988)
38. P. Engstrøm, S. Larrson, A. Rindby, A. Buttkewitz, S. Garbe, G. Gaul, A. Knöchel, F. Lechtenberg, Nucl. Instrum. Methods **A302**, 547 (1991)
39. D.X. Balaic, K.A. Nugent, Z. Barnea, R. Garret, S.W. Wilkins, J. Synchrotron Radiat. **2**, 296 (1995)
40. R. Huang, D. Bilderback, AIP Conf. Proc. **705**, 712 (2003)
41. R. Huang, D. Bilderback, J. Synchrotron Radiat. **13**, 74 (2006)
42. A. Bjeoumikhov, S. Bjeoumikhova, R. Wedell, Part. Part. Syst. Charact. **22**, 384 (2005)
43. J. Bartoll, S. Rohrs, A. Erko, A. Firsov, A. Bjeoumikhov, N. Langhoff, Spectrochim. Acta **B59**, 1587 (2004)
44. A. Knochel, G. Gaul, F. Lechtenberg, German Patent DE 44441092C2, 1994
45. G. Hirsch, J. X-ray Spectrom. **32**, 229 (2003)
46. Y.P. Feng, S.K. Sinha, H.W. Deckman, J.B. Hastings, D.P. Siddons, Phys. Rev. Lett. **71**, 537 (1993)
47. S. Di Fonzo, W. Jark, S. Lagomarsin, C. Giannini, L. De Caro, A. Cedola, M. Muller, Nature **403**, 638 (2000)
48. W. Jark, A. Cedola, S. Di Fonzo, M. Fiordelisi, S. Lagomarsino, N.P. Konovalenko, V.A. Chernov, Appl. Phys. Lett. **78**, 1192 (2001)
49. A. Cedola, S. Lagomarsino, Synchrotron Radiat. News **17**, 30 (2004)
50. F. Pfeiffer, C. David, M. Burghammer, C. Riekel, T. Salditt, Science **297**, 230 (2002)
51. A.V. Baez, J. Opt. Soc. Am. **51**, 405 (1961)
52. B. Lai, W. Yun, D. Legnini, Y. Xiao, J. Chrzas, P.J. Viccaro, V. White, S. Bajikar, D. Denton, F. Cerrina, E. Di. Fabrizio, M. Gentilli, L. Grella, M. Baciocchi, Appl. Phys. Lett. **61**, 1877 (1992)
53. E. Di Fabrizio, M. Gentili, L. Grella, N. Baciocchi, A. Krasniperova, F. Cerina, W. Yun, B. Lai, E. Gluskin, J. Vasc. Sci. Technol. **B12**, 3979 (1994)
54. B. Lai, W. Yun, Y. Xiao, L. Yang, D. Legnini, Z. Cai, A. Krasnoperova, F. Cerrina, E. Di Fabrizio, M. Gentilli, Rev. Sci. Instrum. **66**, 2287 (1995)
55. Z. Chen, Y. Vladimirsky, M. Brown, Q. Leonard, O. Vladimirsky, F. Moore, F. Cerina, B. Lai, W. Yun, E. Gluskin, J. Vasc. Sci. Technol. **B15**, 2522 (1997)
56. W. Yun, S.T. Pratt, R.M. Miller, Z. Cai, D.B. Hunter, A.G. Jarstfer, K.M. Kemner, B. Lai, H.R. Lee, D.G. Legnini, W. Rodrigues, C.I. Smith, J. Synchrotron Radiat. **5**, 1390 (1998)
57. W. Yun, B. Lai, A.A. Krasnoperova, E. Di Fabrizio, Z. Cai, F. Cerina, Z. Chen, M. Gentili, E. Gluskin, Rev. Sci. Instrum. **70**, 3537 (1999)

58. X. Su, C. Stagarescu, G. Xu, D.E. Eastman, I. McNulty, S.P. Frogo, Y. Wang, C.C. Retsch, I.C. Noyan, C.K. Xu, Appl. Phys. Lett. **77**, 3465 (2000)
59. S.D. Shastri, J.M. Maser, B. Lai, J. Tys, Opt. Commun. **197**, 9 (2001)
60. Z. Cai, B. Lai, Y. Xiao, S. Xu, J. Phys. IY France **104**, 17 (2003)
61. K.M. Kemner, S.D. Kelly, B. Lai, J. Maser, E.J. O'Loughlin, D. Sholto-Douglas, Z. Cai, M.A. Schneegurt, C.F. Kulpa, Jr., K.H. Nealson, Science **306**, 686 (2004)
62. J. Maser, G.B. Stephenson, D. Shu, B. Lai, S. Vogt, A. Khounsary, Y. Li, C. Benson, G. Schneider, AIP Conf. Proc. **705**, 470 (2004)
63. L.E. Ocola, J. Maser, S. Vogt, B. Lai, R. Divan, G.B. Stephenson, Proc. SPIE **5539**, 165 (2004)
64. T. Buonassisi, A.A. Istratov, M. Heuer, M.A. Marcus, R. Jonczyk, J. Isenberg, B. Lai, Z. Cai, S. Heald, W. Warta, R. Schindler, G. Willeke, E.R. Weber, J. Appl. Phys. **97**, 074901 (2005)
65. C.C. Abnet, B. Lai, Y.L. Qiao, S. Vogt, X.M. Luo, P.R. Taylor, Z.W. Dong, S.D. Mark, S.M. Dawsey, J. Natl. Cancer Inst. **97**, 301 (2005)
66. T. Buonassisi, M.A. Marcus, A.A. Istratov, M. Heuer, T.F. Ciszek, B. Lai, Z. Cai, E.R. Weber, J. Appl. Phys. **97**, 063503 (2005)
67. Y. Xiao, Z. Cai, Z.L. Wang, B. Lai, Y.S. Chu, J. Synchrotron Radiat. **12**, 124 (2005)
68. H.C. Kang, G.B. Stephenson, C. Liu, R. Conley, A.T. Macrander, J. Maser, S. Bajt, H.N. Chapman, Appl. Phys. Lett. **86**, 151109 (2005)
69. Y. Suzuki, N. Kamijo, S. Tamura, K. Handa, A. Takeuchi, S. Yamamoto, H. Sugiyma, K. Ohsumi, M. Ando, J. Synchrotron Radiat. **4**, 60 (1997)
70. N. Kamijo, S. Tamura, Y. Suzuki, K. Handa, A. Takeuchi, S. Yamamoto, M. Ando, K. Ohsumi, H. Kihara, Rev. Sci. Instrum. **68**, 14 (1997)
71. M. Koike, I.H. Suzuki, S. Komiya, Y. Amemiya, J. Synchrotron Radiat. **5**, 794 (1998)
72. Y. Kagoshima, T. Ibuki, K. Takai, Y. Yokoyama, N. Miyamoto, Y. Tsusaka, J. Matsui, Jpn. J. Appl. Phys. **39**, L433 (2000)
73. Y. Kagoshima, T. Ibuki, Y. Yokoyama, Y. Tsusaka, J. Matsui, K. Takai, M. Aino, Jpn. J. Appl. Phys. **40**, L1190 (2001)
74. Y. Suzuki, A. Takeuchi, H. Takano, T. Ohigashi, H. Takenaka, Jpn. J. Appl. Phys. **40**, 1508 (2001)
75. Y. Kagoshima, T. Ibuki, Y. Yokoyama, K. Takai, Y. Tsusaka, J. Matsui, Jpn. J. Appl. Phys. **41**, 412 (2002)
76. A. Takeuchi, Y. Suzuki, H. Takano, J. Synchrotron Radiat. **9**, 115 (2002)
77. M. Awaji, Y. Suzuki, A. Takeuchi, H. Takano, N. Kamijo, S. Tamura, M. Yasumoto, J. Synchrotron Radiat. **9**, 125 (2002)
78. S. Tamura, M. Yasumoto, N. Kamijo, Y. Suzuki, M. Awaji, A. Takeuchi, H. Takano, K. Handa, J. Synchrotron Radiat. **9**, 154 (2002)
79. N. Kamijo, Y. Suzuki, M. Awaji, A. Takeuchi, H. Takano, T. Ninomiya, S. Tamura, M. Yasumoto, J. Synchrotron Radiat. **9**, 182 (2002)
80. A. Takeuchi, K. Uesugi, H. Takano, Y. Suzuki, Rev. Sci. Instrum. **73**, 4246 (2002)
81. Y. Kagoshima, Y. Yokoyama, T. Ibuki, T. Niimi, Y. Tsusaka, K. Takai, J. Matsui, J, Synchrotron Radiat. **9**, 132 (2002)
82. M. Awaji, A. Takeuchi, H. Takano, N. Kamijo, M. Yasamoto, Y. Terado, S. Tamura, Rev. Sci. Instrum. **74**, 4948 (2003)

83. N. Kamijo, Y. Suzuki, H. Takamo, M. Yasumoto, A. Takeuchi, M. Awaji, Rev. Sci. Instrum. **74**, 5101 (2003)
84. Y. Kagoshima, Y. Yokoyama, T. Niimi, T. Koyama, Y. Tsusaka, J. Matsui, K. Takai, J. Phys. IY France **104**, 49 (2003)
85. Y. Suzuki, M. Awaji, A. Takeuchi, H. Takano, K. Uesugi, Y. Komura, N. Kamijo, M. Yasumoto, S. Tamura, J. Phys. IY France **104**, 35 (2003)
86. Y. Kagoshima, T. Koyama, I. Wada, T. Niimi, Y. Tsusaka, J. Matsui, S. Kimura, M. Kotera, K. Takai, AIP Conf. Proc. **705**, 1263 (2004)
87. Y. Suzuki, A. Takeuchi, H. Takano, K. Uesugi, T. Oka, K. Inoue, Rev. Sci. Instrum. **75**, 1155 (2004)
88. X-Radia website: http://www.xradia.com/
89. NTT website: http://www.ntt-at.com/products_e/x-ray_optics/
90. C. David, B. Kaulich, R. Barrett, M. Solome, J. Susini, Appl. Phys. Lett. **77**, 3851 (2000)
91. C. David, B. Nohammer, E. Ziegler, Microelectron. Eng. **61–62**, 987 (2002)
92. C. David, E. Ziegler, B. Nohammer, J. Synchrotron Radiat. **8**, 1054 (2001)
93. C. David, B. Nohammer, E. Ziegler, Appl. Phys. Lett. **79**, 1088 (2001)
94. H. Solak, C. David, J. Gobrecht, Appl. Phys. Lett. **85**, 2700 (2004)
95. E. Di Fabrizio, F. Romanato, M. Gentili, S. Cabrini, B. Kaulich, J. Susini, R. Barrett, Nature **401**, 895 (1999)
96. B. Kaulich, S. Ostereich, M. Salome, R. Barrett, J. Susini, T. Wilheim, E. Di Fabrizio, M. Gentili, P. Charalambous, Appl. Phys. Lett. **75**, 4061 (1999)
97. T. Wilheim, B. Kaulich, E. Di Fabrizio, S. Cabrini, J. Susini, Appl. Phys. Lett. **78**, 2082 (2001)
98. B. Kaulich, R. Barrett, M. Solome, S. Ostereich, J. Suzini, ESRF Newsletter **34**, 27 (2000)
99. E. Di Fabrizio, D. Cojoc, S. Cabrini, B. Kaulich, J. Susini, P. Facci, T. Wilheim, Opt. Express **11**, 2278 (2003)
100. B. Nohammer, C. David, M. Burghammer, C. Riekel, Appl. Phys. Lett. **86**, 163104 (2005)
101. I. Snigireva, A. Snigirev, G. Vaughan, M. Di Michiel, V. Kohn, V. Yunkin, M. Grigoriev, AIP Conf. Proc. **879**, 998 (2007)
102. I. Snigireva, A. Snigirev, V. Kohn, V. Yunkin, M. Grigoriev, S. Kuznetsov, G. Vaughan, M. Di Michiel, Phys. Stat. Sol. A, to be published
103. D. Rudolph, G. Schmahl, B. Niemann, Proc. SPIE **316**, 103 (1982)
104. W. Yun, M. Feser, A. Lyon, F. Duewer, Y. Wang, Proc. SPIE **5539**, 133 (2004)
105. O. Tatchyn, in *X-ray Microscopy*, ed. by G. Schmahl, D. Rudolph, Springer Series in Optical Sciences, vol. 43 (Springer, Berlin Heidelberg New York, 1990), p. 40
106. A. Snigirev, V. Kohn, I. Snigireva, B. Lengeler, Nature **384**, 49 (1996)
107. A. Snigirev, V. Kohn, I. Snigireva, A. Souvorov, B. Lengeler, Appl. Opt. **37**, 653 (1998)
108. B. Lengeler, J. Tummler, A. Snigirev, I. Snigireva, C. Raven, J. Appl. Phys. **84**, 5855 (1998)
109. P. Elleaume, ESRF Newsletter **28**, 33 (1997)
110. A. Snigirev, B. Filseth, P. Elleaume, Th. Kolocke, V. Kohn, B. Lengeler, I. Snigireva, A. Souvorov, J. Tummler, Proc. SPIE **3151A**, 164 (1997)
111. P. Elleaume, J. Synchrotron Radiat. **5**, 1 (1998)
112. P. Elleaume, Nucl. Instrum. Methods **A412**, 483 (1998)

113. A. Chumakov, R. Ruffer, O. Leupold, A. Barla, H. Thiess, T. Asthalter, P. Doyle, A. Snigirev, A. Baron, Appl. Phys. Lett. **77**, 31 (2000)
114. A.Q. Baron, Y. Kohmura, Y. Ohishi, T. Ishikawa, Appl. Phys. Lett. **74**, 1492 (1999)
115. A.Q.R. Baron, Y. Kohmura, V.V. Krishnamurthy, Yu.V. Shvyd'ko, T. Ishikawa, J. Synchrotron Radiat. **6**, 953 (1999)
116. B. Lengeler, C.G. Schroer, M. Richwin, J. Tummler, M. Drakopoulos, A. Snigirev, I. Snigireva, Appl. Phys. Lett. **74**, 3924 (1999)
117. B. Lengeler, C. Schroer, J. Tummler, B. Benner, M. Richwin, A. Snigirev, I. Snigireva, M. Drakopoulos, J. Synchrotron Radiat. **6**, 1153 (1999)
118. B. Lengeler, C. Schroer, J. Tummler, B. Benner, M. Richwin, A. Snigirev, I. Snigireva, M. Drakopoulos, Synchrotron Radiat. News **12**(5), 45 (1999)
119. C.G. Schroer, J. Tummler, F. Gunzler, B. Lengeler, W.H. Schroder, A.J. Kuhn, A. Simionovici, A. Snigirev, I. Snigireva, Proc. SPIE **4142**, 287 (2000)
120. B. Lengeler, C. Schroer, B. Benner, F. Gunsler, M. Kuhlmann, J. Tummler, A. Simionovici, M. Drakopoulos, A. Snigirev, I. Snigireva, Nucl. Instrum. Methods A **467–468**, 944 (2001)
121. C. Schroer, F. Gunsler, B. Benner, M. Kuhlmann, J. Tummler, B. Lengeler, C. Rau, T. Weitkamp, A. Snigirev, I. Snigireva, Nucl. Instrum. Methods A **467–468**, 966 (2001)
122. C. Schroer, B. Benner, F. Gunzler, M. Kuhlmann, C. Zimprich, B. Lengeler, C. Rau, T. Weitkamp, A. Snigirev, I. Snigireva, J. Appenzeller, Rev. Sci. Instrum. **73**, 1640 (2002)
123. C.G. Schroer, J. Meyer, M. Kuhlmann, B. Benner, T.F. Gunsler, B. Lengeler, C. Rau, T. Weitkamp, A. Snigirev, I. Snigireva, Appl. Phys. Lett. **81**, 1527 (2002)
124. C.G. Schroer, M. Kuhlmann, B. Lengeler, T.F. Gunsler, O. Kurapova, B. Benner, C. Rau, A.S. Simionovici, A. Snigirev, I. Snigireva, Proc. SPIE **4783**, 10 (2002)
125. H. Reichert, V. Honkimaki, A. Snigirev, S. Engemann, H. Dosch, Physica B **336**, 46 (2003)
126. S. Engemann, H. Reichert, H. Dosch, J. Bilgram, V. Honimaki, A. Snigirev, Phys. Rev. Lett. **92**, 205701 (2004)
127. C. Mocuta, H. Reichert, K. Mecke, H. Dosch, M. Drakopoulos, Science **308**, 1287 (2005)
128. V. Aristov, M. Grigoriev, S. Kuznetsov, L. Shabelnikov, V. Yunkin, T. Weitkamp, C. Rau, I. Snigireva, A. Snigirev, M. Hoffmann, E. Voges, Appl. Phys. Lett. **77**, 4058 (2000)
129. V. Aristov, M. Grigoriev, S. Kuznetsov, L. Shabelnikov, V. Yunkin, C. Rau, A. Snigirev, I. Snigireva, T. Weitkamp, M. Hoffmann, E. Voges, Proc. SPIE **4145**, 285 (2001)
130. I. Snigireva, A. Snigirev, C. Rau, T. Weitkamp, V. Aristov, M. Grigoriev, S. Kuznetsov, L. Shabelnikov, V. Yunkin, M. Hoffmann, E. Voges, Nucl. Instrum. Methods A **467–468**, 982 (2001)
131. M. Grigoriev, L. Shabelnikov, V. Yunkin, A. Snigirev, I. Snigireva, M. Di Michiel, S. Kuznetsov, M. Hoffmann, E. Voges, Proc. SPIE **4501**, 185 (2001)
132. I. Snigireva, M. Grigoriev, L. Shabelnikov, V. Yunkin, A. Snigirev, S. Kuznetsov, M. Di Michiel, M. Hoffmann, E. Voges, Proc. SPIE. **4783**, 19 (2002)

133. M. Drakopoulos, J. Zegenhagen, A. Snigirev, I. Snigireva, M. Hauser, K. Eberl, V. Aristov, L. Shabelnikov, V. Yunkin, Appl. Phys. Lett. **81**, 2279 (2002)
134. M. Drakopoulos, J. Zegenhagen, T.-L. Lee, A. Snigirev, I. Snigireva, V. Cimalla, O. Ambacher, J. Phys. D: Appl. Phys. **36**, A214 (2003)
135. M. Drakopoulos, J. Zegenhagen, A. Snigirev, I. Snigireva, Synchrotron Radiat. News **17**(3), 37 (2004)
136. C.G. Schroer, M. Kuhlmann, U.T. Hunger, T.F. Gunsler, O. Kurapova, S. Feste, F. Frehse, B. Lengeler, M. Drakopoulos, A. Somogyi, A.S. Simionovici, A. Snigirev, I. Snigireva, C. Schug, W.H. Schroder, Appl. Phys. Lett. **82**, 1485 (2003)
137. C.G. Schroer, B. Benner, T.F. Günzler, M. Kuhlmann, J. Patommel, B. Lengeler, A. Somogyi, T. Weitkamp, C. Rau, A. Snigirev, I. Snigireva, Proc. SPIE **5535**, 701 (2004)
138. C.G. Schroer, T.F. Günzler, M. Kuhlmann, O. Kurapova, S. Feste, M. Schweitzer, B. Lengeler, W.H. Schröder, A. Somogyi, A.S. Simionovici, A. Snigirev, I. Snigireva, Proc. SPIE **5535**, 162 (2004)
139. A. Snigirev, V. Yunkin, I. Snigireva, M. Di Michiel, M. Drakopoulos, S. Kouznetsov, L. Shabelnikov, M. Grigoriev, V. Ralchenko, I. Sycho, M. Hoffmann, E. Voges, Proc. SPIE **4783**, 1 (2002)
140. B. Nohamme, J. Hoszowska, A.K. Freund, C. David, J. Synchrotron Radiat. **10**, 168 (2003)
141. V. Nazmov, E. Reznikova, M. Boerner, J. Mohr, V. Saile, A. Snigirev, I. Snigireva, M. Di Michie, M. Drakopoulos, R. Simon, M. Grigoriev, AIP Conf. Proc. **705**, 752 (2004)
142. A. Snigirev, I. Snigireva, M. Di Michiel, V. Honkimaki, M. Grigoriev, V. Nazmov, E. Reznikova, J. Mohr, V. Saile, Proc. SPIE **5539**, 244 (2004)
143. A. Mazuelas, A. Snigirev, I. Snigireva, C. David, P. Boesecke, H. Djazouli, T.H. Metzger, Proc. SPIE **5539**, 259 (2004)
144. B. Struth, A. Snigirev, O. Konovalov, A. Otten, R. Gauggel, T. Phohl, AIP Conf. Proc. **705**, 804 (2004)
145. C. Bergemann, H. Keymeulen, J.F. Van der Veen, Phys. Rev. Lett. **91**, 204801 (2003)
146. C. Schroer, B. Lengeler, Phys. Rev. Lett. **94**, 054802 (2005)
147. C.G. Schroer, Phys. Rev. B **74**, 033405 (2006)
148. F. Pfeiffer, C. David, J.F. van der Veen, C. Bergemann, Phys. Rev. B **73**, 245331 (2006)